




Aerodynamic shape optimization of airfoils at ultra-low Reynolds numbers

MEEDHU GEOGY UKKEN and M SIVAPRAGASAM*

Department of Automotive and Aeronautical Engineering, Faculty of Engineering and Technology, M S Ramaiah University of Applied Sciences, Bangalore 560 058, India
e-mail: sivapragasam.aae.et@msruas.ac.in

MS received 13 May 2018; revised 24 October 2018; accepted 25 March 2019; published online 3 May 2019

Abstract. The flow over NACA 0008 airfoil is studied computationally in the ultra-low Reynolds number regime $Re \in [1000, 10000]$ for various angles of attack $\alpha \in [0^\circ, 8^\circ]$. The laminar flow separation occurs even at low angles of attack in this Reynolds number regime. The lift curve slope is far reduced from the inviscid thin airfoil theory value of $C_{l,\alpha} = 2\pi$. Significant increase in the values of drag coefficient is seen with a decrease in Re . Lift-to-drag ratios are consequently very low. An adjoint-based aerodynamic shape optimization methodology is employed to obtain improved aerodynamic characteristics in the ultra-low Re regime. Three different objective functions are considered, namely, (i) minimization of drag coefficient, C_d , (ii) maximization of lift coefficient, C_l , and (iii) maximization of lift-to-drag ratio, (C_l/C_d) . Significant improvement in each of the objective functions is obtained.

Keywords. Ultra-low Reynolds number flow; NACA 0008 airfoil; aerodynamic shape optimization; adjoint method.

1. Introduction

The recent interest in micro- [1], nano- [2] and pico-air vehicles [3] has motivated research in the study of aerodynamics at low Reynolds numbers. Particularly, DARPA specifications for nano-air vehicles with extremely small wing span of less than 7.5 cm and capable of efficient flight at Reynolds numbers (Re) less than 15,000, and pico-air vehicles operating at $Re < 3000$ are worth mentioning. The flight regime of many insects and small birds is also in this Reynolds number range. Thus, the study of aerodynamics at low Reynolds numbers becomes pertinent for both natural and engineered flying objects. In fact, the distinction between these flyers is diminishing with the advent of biologically inspired flight vehicles.

Extensive reviews of aerodynamic phenomena at low Reynolds numbers have appeared [4–7]; compendiums of airfoil aerodynamic data in the Reynolds number range 20,000 to 5×10^5 are also available [8]. However, airfoil data below this range are rather sparse [9–12]. Of particular interest here, is the range $Re \in [1000, 10000]$. This Re regime is termed ultra-low. At such low Reynolds numbers the flow is dominated by viscous effects. The laminar boundary layers have a tendency to separate even with mild adverse pressure gradients leading to laminar flow separation and, perhaps, reattachment. The separated flow

significantly alters the effective geometry of the airfoil and thus its aerodynamics. With low values of lift coefficients, and high drag coefficients, very low values of lift-to-drag ratios are obtained. This fact provides a motivation for designing airfoils for improved aerodynamic characteristics at such low Re .

Optimization procedures offer an attractive proposition for aerodynamic design. In the past several optimization techniques have been applied in aerodynamic design with gradient-based methods being the earliest [13]. However, such methods have an intrinsic disadvantage. The determination of the sensitivity of the objective function, say, for example, drag minimization, with respect to the design variables calls for repetitive computations of the flow field with concomitant huge computational costs. This disadvantage can be eliminated by formulating the optimization problem in the framework of calculus of variations/optimal control theory. In such methods the flow field equations are adjoined to the objective function using a Lagrange multiplier. The gradient of the objective function can thus be obtained by solving the resulting adjoint equation, thereby greatly reducing the computational cost. Such methods provide an appealing and economic framework for design optimization when the number of design variables is particularly large. Pironneau's [14] pioneering effort in this field is worth mentioning. In aeronautical applications, the work of Jameson [15] has been seminal. An excellent introduction to the adjoint methods is Pierce and Giles [16],

*For correspondence

and a nice review on aerodynamic shape optimization in general, is Mohammadi and Pironneau [17].

In the light of the above discussion, the main objectives of this study are two-fold. Firstly, to evaluate the aerodynamic characteristics of NACA 0008 airfoil in the ultra-low range $Re \in [1000, 10000]$. Secondly, to obtain optimal airfoil shapes resulting from aerodynamic shape optimization for three different objective functions, namely, (i) minimization of drag coefficient, C_d , (ii) maximization of lift coefficient, C_l , and (iii) maximization of lift-to-drag ratio, (C_l/C_d) , in this Re range. The present paper is arranged as follows. The computational procedure is given in section 2. The aerodynamic characteristics of NACA 0008 airfoil is presented in detail subsequently in section 3. The aerodynamic shape optimization procedure is presented briefly in section 4, and then the results of the three different objective functions are discussed in section 5. Finally, conclusions are given in section 6.

2. Computational procedure and validation

In this section, the procedure for numerically computing the flow field over NACA 0008 airfoil is presented. This airfoil was chosen for the present computations since some computational results were available [11, 12]. The laminar, steady-state Navier–Stokes equations

$$\begin{aligned} \nabla \cdot \mathbf{u} &= 0, \\ \mathbf{u} \cdot \nabla \mathbf{u} &= -\frac{1}{\rho} \nabla p + \nu \nabla^2 \mathbf{u} \end{aligned} \quad (1)$$

are solved numerically using the finite-volume method-based computational code Fluent. Here \mathbf{u} is the velocity vector, ρ is the uniform fluid density, p is the pressure and ν is the fluid kinematic viscosity. For the computations a structured grid of C-grid topology was generated around the airfoil. The radius of the computational domain was $10c$ measured from the leading edge of the airfoil and the domain extended $20c$ behind the leading edge of the airfoil; c is the airfoil chord length. Care was taken in generating a good quality grid keeping in mind the flow features that were to be resolved. A close-up view of the grid surrounding the airfoil is shown in figure 1.

At the inlet of the computational domain, velocity inlet boundary condition was imposed. The velocity was calculated based on the desired Re . Pressure outlet boundary condition was applied at the exit of the computational domain. The no-slip boundary condition was applied on the airfoil surface. The convective terms in the Navier–Stokes equations (1) were discretized by a second-order upwind scheme and the viscous terms by a second-order central differencing scheme. All calculations were done in double-precision arithmetic. The convergence of the residuals was 10^{-6} . The convergence of the residuals for a typical case

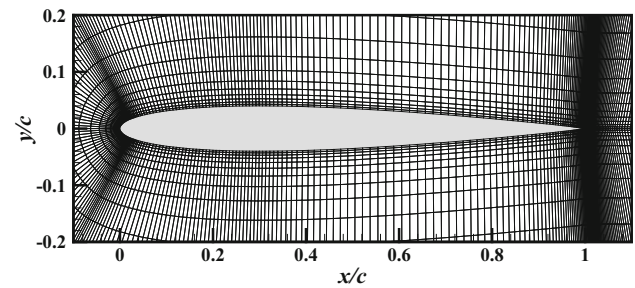


Figure 1. A close-up view of the grid surrounding the airfoil. Shown here is the medium grid with 288 grid points on the airfoil surface.

$Re = 2000$ and angle of attack, $\alpha = 2^\circ$ is shown in figure 2a, and the convergence of the aerodynamic force coefficients in figure 2b.

The number of grid points for computations was chosen after a careful grid independence study. This study was done for $Re = 2000$ at an angle of attack, $\alpha = 4^\circ$ with 12,744 (coarse grid, with 142 grid points on the airfoil surface), 26,513 (medium, 288) and 46,584 (fine, 378) cells. The pressure and skin friction distributions over the airfoil were plotted (not shown here for the sake of brevity) for the results from these three grids. The results were found to be convincingly grid independent. Further, to formally quantify the discretization error, the Grid Convergence Index (GCI) [18] was calculated for C_l and C_d . The numerical uncertainty in the evaluation of C_l was 0.718% and 0.578% for the coarse-medium and medium-fine grids, respectively. Similarly, values for C_d were 0.115% and 0.025%. Since the medium grid had a comparatively low value of discretization error it was chosen for all subsequent computations.

In the present study, the flow field was assumed to be steady. At ultra-low Reynolds numbers and low angles of attack the flow nominally remains steady and the precise values of Re and α at which the flow starts exhibiting significant unsteady behaviour is unknown. We performed unsteady computations for an impulsively started NACA 0008 airfoil at $Re = 2000$ and $\alpha = 2^\circ$ with a time step of $\Delta t = 1 \times 10^{-3}$ s and numerically integrated the unsteady Navier–Stokes equations for 1000 time steps which corresponded to a total physical time of $t = 1.0$ s. The unsteady numerical formulation was second-order implicit. The convergence of the residuals was set to 10^{-5} for every time step. The time history of the aerodynamic force coefficients is shown in figure 3. In this figure T is the period of time-integration. It can be seen that both C_l and C_d do indeed reach their steady-state values of 0.142 and 0.077, respectively, shown by thin horizontal lines in figure 3. It is reassuring to see that a steady-state solution exists. It must be mentioned here that the numerical time-integration to achieve a steady-state solution takes more than 140 hours computation time on a computing workstation. The

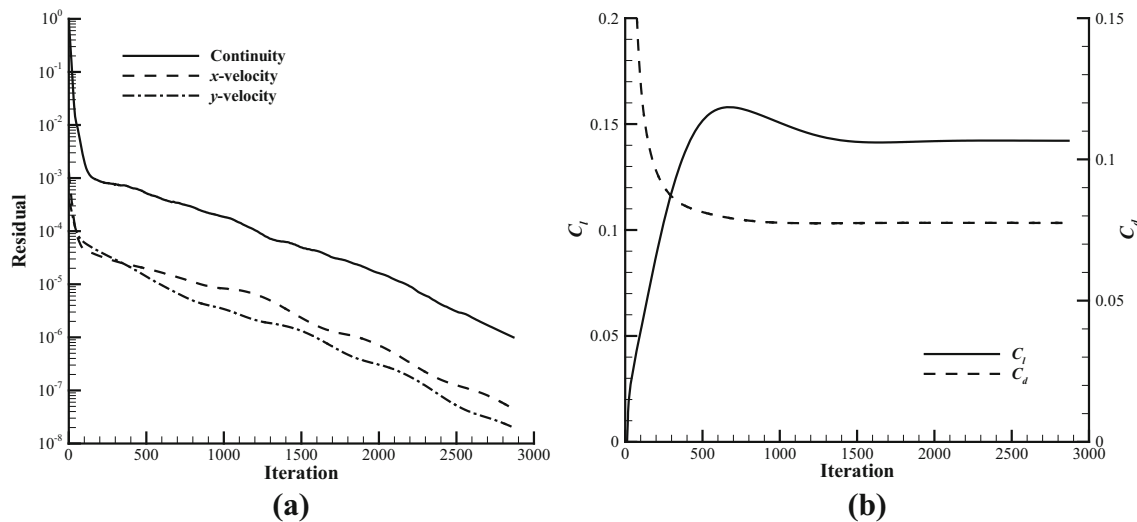


Figure 2. Convergence of (a) residuals and (b) aerodynamic force coefficients; $Re = 2000$ and $\alpha = 2^\circ$.

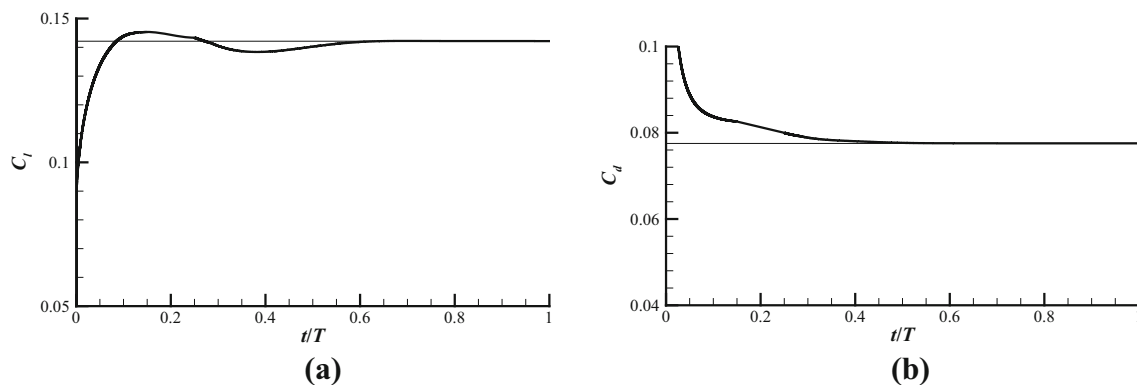


Figure 3. Time history of (a) C_l and (b) C_d ; $Re = 2000$ and $\alpha = 2^\circ$.

assumption of steady flow results in significant computational time advantage.

The computed pressure distribution over the NACA 0008 airfoil at $Re = 2000$ and $\alpha = 2^\circ$ is compared with the available computations [11, 12, 19] in figure 4. The agreement is good, indicating a validation of the present computational procedure.

3. Aerodynamic characteristics of NACA 0008 airfoil

In this section, we present detailed results of the aerodynamic characteristics of NACA 0008 airfoil in the ultra-low range $Re \in [1000, 10000]$. In an earlier study [19], we presented elaborate results at $Re = 2000$ and 6000, and the present data complements our previous work. The pressure distribution on the airfoil at $\alpha = 0^\circ$ and 4° are plotted in figure 5. The inviscid pressure distribution, calculated

using a panel code with 100 panels, is also plotted for comparison. The effect of Reynolds number on the pressure distribution on the airfoil at zero incidence can be seen in figure 5a. At zero incidence the flow remained attached at all Re . The pressure distribution near the leading edge is smooth due to viscous effects. The slope of the adverse pressure gradient increases with an increase in Reynolds number. A decrease in the negative pressure coefficient is noted near the trailing edge at lower Re .

The pressure distribution at $\alpha = 4^\circ$ is now considered. The pressure distribution, in fact for all angles of attack, exhibits a marked departure from their inviscid behaviour. The flow accelerates rapidly around the leading edge causing the pressure to decrease precipitously on the upper surface to a minimum value within 5 percent of the airfoil chord and moving closer to the leading edge as the angle of attack increases. The steep favourable pressure gradient near the leading edge of the airfoil seen in the inviscid pressure distribution is not observed at low Re because of

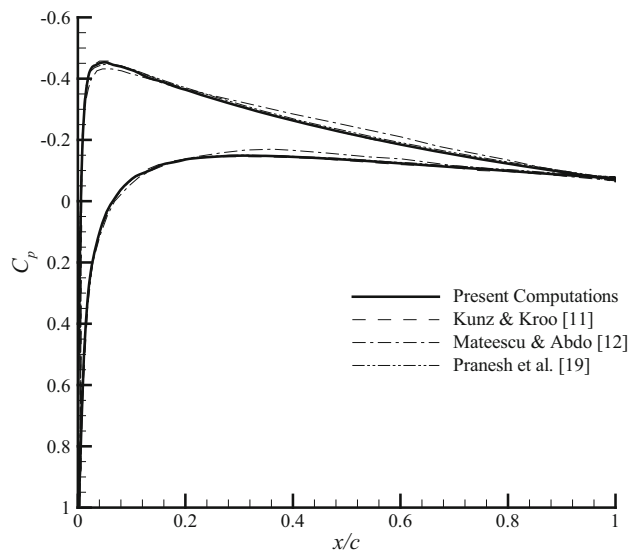
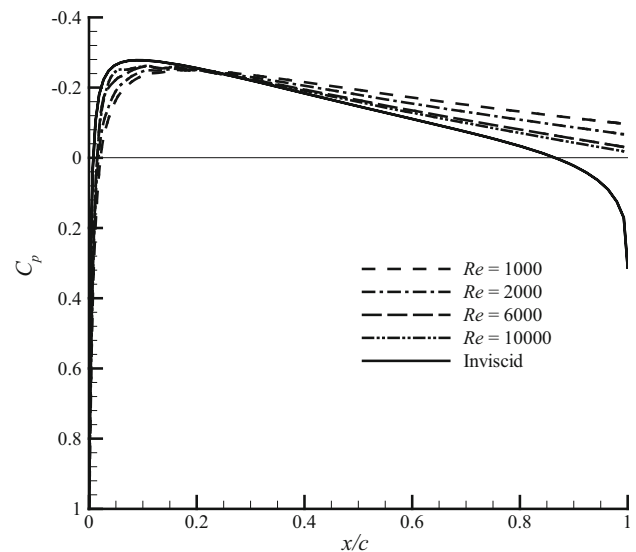


Figure 4. Pressure distribution over the NACA 0008 airfoil at $Re = 2000$ and $\alpha = 2^\circ$.

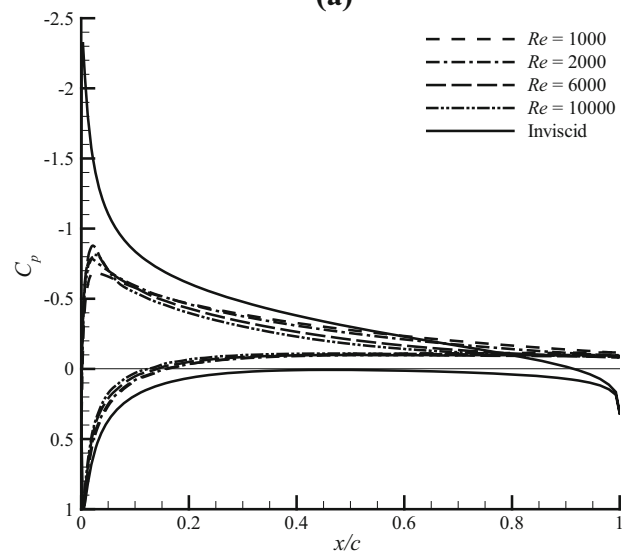
viscous effects. The magnitude of minimum pressure is also reduced in the viscous flow cases. The pressure recovery from the minimum value to that at the trailing edge is smooth in the viscous flow. In the region of pressure recovery the slope of the adverse pressure gradient is lower compared to the inviscid value. At the trailing edge the pressure is lower than the freestream pressure for the viscous flow and the pressure gradient is not as severe as in their inviscid counterpart.

The viscous effects become predominant at very low Reynolds numbers and thick boundary layers develop over the airfoil, which can be a significant fraction of chord length, with a tendency to separate even at a small angle of attack. The flow separation and reattachment locations, x_s/c and x_r/c , respectively, were determined from the shear stress distribution on the airfoil upper surface. For all the cases considered here flow remained attached on the lower surface. While we tabulate x_s/c and x_r/c for $Re = 2000$ in table 1, for other Re they are collectively plotted in figure 6. In table 1, l_s is the length of the separated region. The onset of flow separation is at $\alpha = 6^\circ$ for $Re = 1000$, and occurs at lower α for increasing Re . Once the flow separates, as the angle of attack increases the separation point moves closer to the leading edge. The development of the separated region is retarded at lower Reynolds numbers. The separated flow eventually reattaches at a location close to the trailing edge. The separated region covers a significant portion of the airfoil chord particularly at higher α .

We display in figure 7 some streamline plots to illustrate how the flow field over the airfoil changes with an increase in angle of attack for a few Re . At $\alpha = 0^\circ$ the streamlines are only perturbed slightly from the freestream pattern. As the angle of attack increases the stagnation point moves downstream of the airfoil leading edge on the lower



(a)



(b)

Figure 5. Pressure distribution over NACA 0008 airfoil at (a) $\alpha = 0^\circ$ and (b) $\alpha = 4^\circ$ for various Re .

surface. At higher angles of attack a large recirculation bubble, whose thickness is much higher than the maximum thickness of the airfoil, appears near the trailing edge and remains attached to the airfoil. A further interesting feature is the appearance of two eddies at higher α and higher Re . The occurrence of two, or even more eddies is not quite uncommon in low Reynolds number flow fields.

The lift curves for the NACA 0008 airfoil are plotted in figure 8. The present results agree well with the available computations [11, 12] but not shown here for the sake of brevity. Several interesting and important observations can be made from figure 8. The lift curve slope is far reduced from the inviscid thin airfoil theory value of $C_{l,\alpha} = 2\pi$. The magnitude of C_l is about half of those at very high Re ;

Table 1. Flow separation and reattachment locations on the airfoil for $Re = 2000$.

	x_s/c	x_r/c	l_s/c
0°	No separation		
1°			
2°			
3°			
4°	0.898 (0.900) ^a	0.987	0.089
5°	0.676 (0.680)	0.991	0.315
6°	0.483 (0.490) {0.5015} ^b	0.991 {0.9870}	0.508 {0.4855}
7°	0.333	0.990	0.657
8°	0.233	0.986	0.753

^aValues in parentheses (-) are from Kunz and Kroo [11]. The reattachment location is not specified there, but we infer from their streamline plots that it is very close to the trailing edge.

^bValues in braces {-} are from Mateescu and Abdo [12].

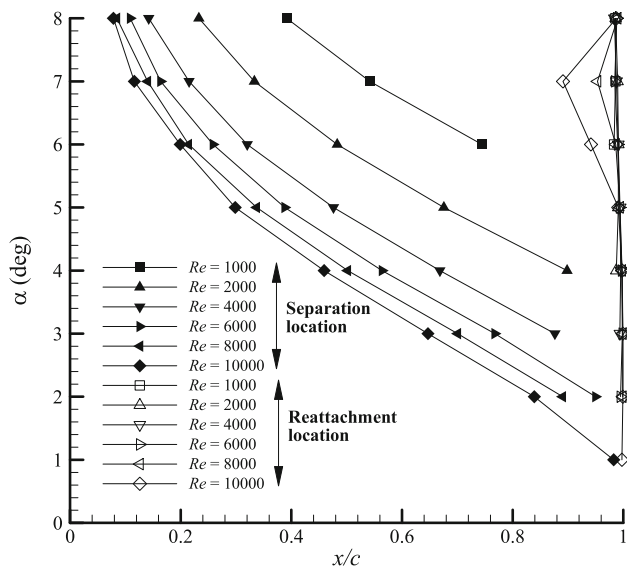


Figure 6. Flow separation and reattachment locations on the airfoil. The filled symbols represent the separation location, and the open symbols the reattachment location.

aerodynamic data for this airfoil at $Re = 1.5 \times 10^6$ to 6×10^6 can be found in McCullough [20]. We had seen earlier in figure 6 that the onset of flow separation occurs at a higher angles of attack for lower Reynolds number. The range of the linear portion of C_l - α curve is thus extended to higher α as Re is reduced. After flow separation C_l increases, though not in a linear manner, till the airfoil eventually stalls. This stalling behaviour is very mild.

Further, we observe higher values of C_l at lower Re . This fact, at first sight, is rather surprising. Low Reynolds number flows can spring quite a few surprises! We explain this unusual lift characteristic as follows. Consider, for example, $\alpha = 4^\circ$ for $Re = 2000$ and 6000 for which the flow

separation region is shown in figure 9. The separated flow alters the effective geometry of the airfoil, and consequently its effective camber. The effective camber is also shown in figure 9. $Re = 6000$ case exhibits a larger separated region and a pronounced reflex camber starting at $x/c = 0.6$. The net effect of this reflex camber is to produce a lower C_l than that achieved at a lower Re .

The drag curves are plotted in figure 10. The C_d values are much larger than at high Re . The C_d values at $Re = 2000$ are approximately 40% larger than at $Re = 6000$ even in the linear range of the lift curve, whereas such drastic variation in C_d with Re is not observed at high Reynolds numbers. For all the Reynolds numbers considered here the viscous component of drag is significant and it continuously decreases with increasing angle of attack, while the contribution due to pressure drag increases, as is expected, due to flow separation effects. The zero-lift drag coefficient decreases with an increase in Reynolds number, and closely follows the $1/\sqrt{Re}$ relation.

To summarize, in the ultra-low Re regime, C_l values are low, and with high values of C_d , values of (C_l/C_d) are low, which are in fact an order-of-magnitude lower than that can be obtained at high Reynolds numbers. This provides a motivation for designing airfoils for improved aerodynamic characteristics at low Re , and leads us to the next major theme of this paper.

4. Aerodynamic optimization procedure

In this section, we present the adjoint-based aerodynamic optimization methodology. Our exposition here is standard, and hence brief. Consider the flow over an airfoil, for which the aerodynamic properties defining the objective function, I , are the flow field variables, ω , and the physical location of the boundary, ζ . Then, I , can be defined as

$$I = I(\omega, \zeta). \tag{2}$$

A change in ζ results in a change in I as

$$\delta I = \left[\frac{\partial I}{\partial \omega} \right] \delta \omega + \left[\frac{\partial I}{\partial \zeta} \right] \delta \zeta. \tag{3}$$

Now, if the governing equation, \mathbf{R} , which expresses the dependence on ω and ζ can be written as

$$\mathbf{R}(\omega, \zeta) = 0 \tag{4}$$

then, $\delta \omega$ can be determined from

$$\delta \mathbf{R} = \left[\frac{\partial \mathbf{R}}{\partial \omega} \right] \delta \omega + \left[\frac{\partial \mathbf{R}}{\partial \zeta} \right] \delta \zeta = 0. \tag{5}$$

At this stage the method of Lagrange multiplier, with ψ as the multiplier, is introduced which converts a constrained optimization problem into an unconstrained one.

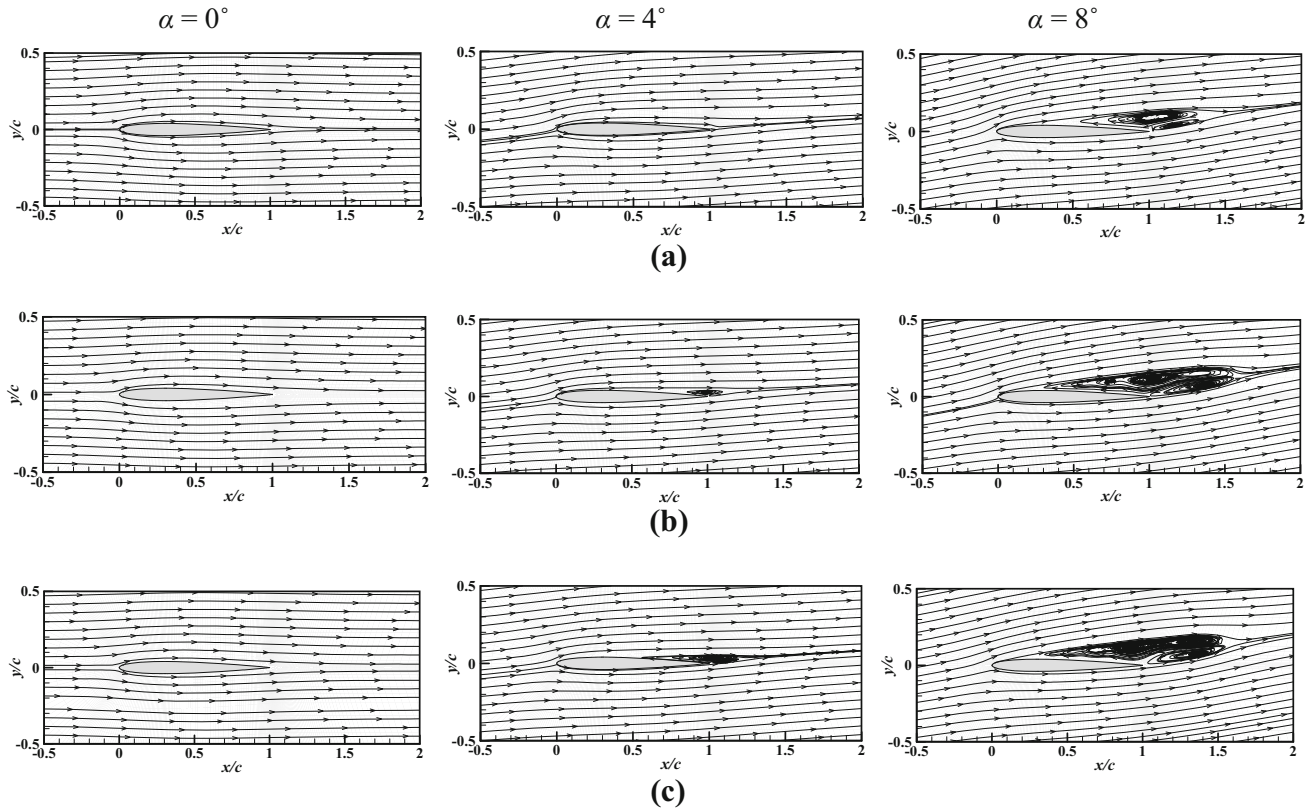


Figure 7. Streamlines over the airfoil at $\alpha = 0^\circ, 4^\circ$ and 8° for (a) $Re = 2000$, (b) $Re = 6000$, and (c) $Re = 10000$.

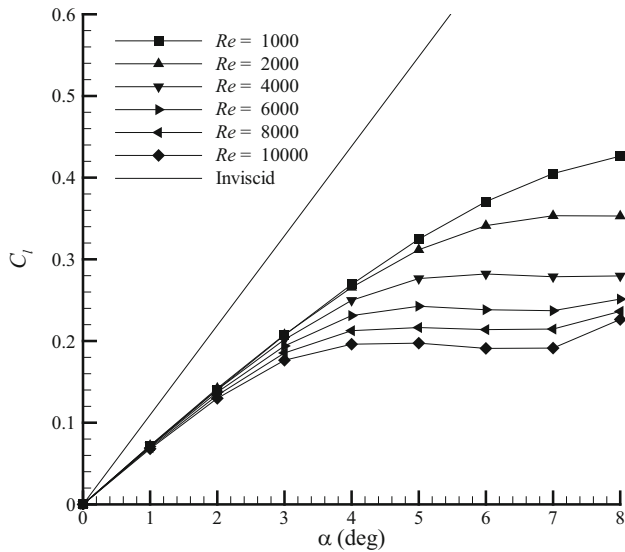


Figure 8. Variation of lift coefficient with angle of attack.

Moreover, since the variation in δR is zero, it can be multiplied by ψ and subtracted from the variation δI without changing the result. So Eq. (3) can be written as

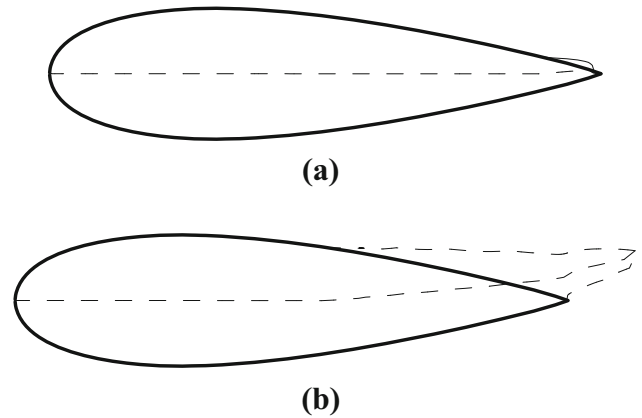


Figure 9. Flow separation region (contour line of axial velocity, $u_x = 0$) and effective camber for (a) $Re = 2000$, and (b) $Re = 6000$; $\alpha = 4^\circ$ in both the cases. In these figures the vertical axis is stretched and displayed for clarity.

$$\begin{aligned} \delta I &= \left[\frac{\partial I^T}{\partial \omega} \right] \delta \omega + \left[\frac{\partial I^T}{\partial \zeta} \right] \delta \zeta - \psi^T \left(\left[\frac{\partial R}{\partial \omega} \right] \delta \omega + \left[\frac{\partial R}{\partial \zeta} \right] \delta \zeta \right) \\ &= \left\{ \left[\frac{\partial I^T}{\partial \omega} \right] - \psi^T \left[\frac{\partial R}{\partial \omega} \right] \right\} \delta \omega + \left\{ \left[\frac{\partial I^T}{\partial \zeta} \right] - \psi^T \left[\frac{\partial R}{\partial \zeta} \right] \right\} \delta \zeta. \end{aligned} \tag{6}$$

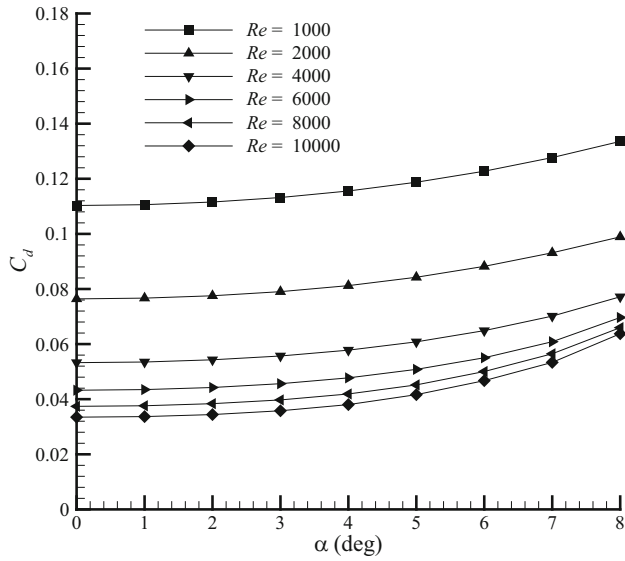


Figure 10. Variation of drag coefficient with angle of attack.

Now ψ has to be chosen such that it satisfies the adjoint equation.

$$\left[\frac{\partial \mathbf{R}}{\partial \omega} \right]^T \psi = \frac{\partial I}{\partial \omega}. \quad (7)$$

Substituting the adjoint equation in Eq. (6) leads to a relation between I and ζ .

$$\delta I = G \delta \zeta \quad (8)$$

where

$$G = \left[\frac{\partial I^T}{\partial \zeta} \right] - \psi^T \left[\frac{\partial \mathbf{R}}{\partial \zeta} \right].$$

The optimal solution is said to have been achieved when the gradient of the augmented objective function approaches zero, i.e., $\delta I = 0$. Based on these equations the adjoint solver computes the sensitivity of the specified objective function to the geometric shape of the airfoil.

Some remarks are in place here. Firstly, the greatest advantage with the adjoint method is evident by an examination of Eq. (8). This equation is independent of ω and thus the gradient of I can be determined with respect to an arbitrarily large number of design variables by solving this equation once. Secondly, in the present case the governing equation \mathbf{R} is the non-linear Navier–Stokes equations, but the adjoint equation is linear. However, the dimension of both the equations are the same. This indicates that the computational cost of solving the adjoint equations is the same as that of the flow equations. Thirdly, in the present paper we employ the discrete formulation of the adjoint system, where the non-linear governing equation is discretized and the adjoint equations derived for the

discretized form of the governing equations. In the continuous adjoint approach, on the other hand, starting from the governing differential equations, the adjoint equations are derived and then discretized. Either approach has its own merits and demerits, but in principle, with sufficiently smooth solutions and in the limit of infinitesimally small grid spacing they should converge to the correct analytic value for the gradient of I [16].

In the present paper the discrete adjoint solver implemented in Fluent is used for aerodynamic optimization. Three different objective functions are considered, namely, (i) minimizing C_d at $\alpha = 0^\circ$, i.e., C_{d0} , (ii) maximizing C_l at $\alpha = 2^\circ$, and (iii) maximizing (C_l/C_d) at $\alpha = 2^\circ$, for $Re \in [1000, 10000]$. The initial body shape for the optimization process is the NACA 0008 airfoil. The design process employed is illustrated by means of a flow chart in figure 11. The adjoint continuity equation was discretized by a first-order upwind scheme, and the adjoint momentum equations by a second-order upwind scheme. The convergence of the residuals of the adjoint quantities was set to

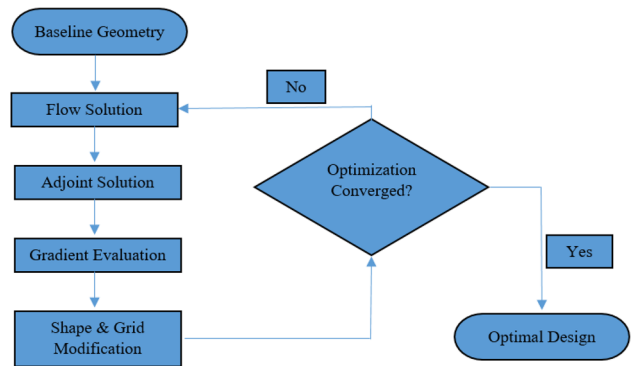


Figure 11. Optimal airfoil design cycle.

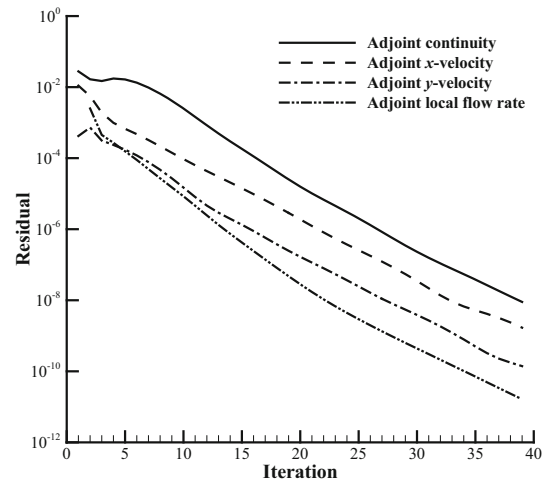


Figure 12. Typical residual convergence of the adjoint solver.

10^{-8} . Example convergence of the adjoint residuals is shown in figure 12 for one iterative step in the design process.

In the design process, as the airfoil geometry is changed a new grid is generated by a mesh morphing scheme which ensures smooth repositioning of the grid points [21]. Convergence is said to have occurred when there is no further improvement in the values of the objective function with design iterations. Flow computations typically took about 15 minutes wall-clock time on a Lenovo Workstation with 8 GB RAM and Intel i5, 3.10 GHz speed processor. Each adjoint solution approximately took about the same wall-clock time. The time periods quoted here are for one iterative step in the design process. The optimal designs were attained within about 40 design iterations.

5. Optimal airfoil shapes

In this section the optimal airfoil shapes obtained for each of the three objective functions is presented and discussed.

5.1 Minimizing C_{d0}

The first problem of interest is to determine the shape of a minimum drag body for $Re \in [1000, 10000]$. Certain constraints were imposed during the design cycle. The airfoil chord length was maintained at $x/c = 1$ throughout the design process by fixing the leading and trailing edges. It was also maintained that the upper and lower surfaces of the airfoil do not intersect. A geometrical constraint on the area of the airfoil was also imposed for this objective function such that the area is lower-bounded by A_{ref} . Starting from the NACA 0008 airfoil the flow and adjoint computations were carried out as in figure 11. The convergence history of the objective function, for example, for $Re = 2000$ is shown in figure 13. We see that C_d decreases monotonically with design iterations. The evolution of the airfoil shapes as the design process progresses is also depicted in figure 13. The optimal airfoil shown in figure 14 at $Re = 2000$ had $C_d = 0.0728$ which is 4.7% (about 36 drag counts) less than the NACA 0008 airfoil. The reduction in C_d is brought about by a reduction in pressure contribution to C_d . A small reduction in viscous contribution to C_d was also obtained. The purpose of streamlining a body is indeed to reduce the pressure contribution to the total drag, and the present optimization procedure is able to achieve this.

The optimal airfoil obtained by Kondoh *et al* [22] for $Re = 2000$ is also shown in figure 14. The resemblance between these shapes is striking. It may be mentioned here that Kondoh *et al* [22] performed topology optimization using the adjoint sensitivities and SQP optimization algorithm to obtain their optimal shape which had $C_d = 0.075$. The optimal airfoil shapes obtained at other Re in the

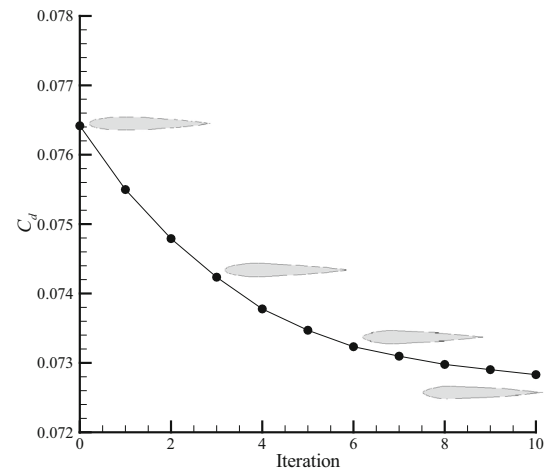


Figure 13. Convergence history of C_d minimization and evolution of airfoil shapes with design iterations for $Re = 2000$.

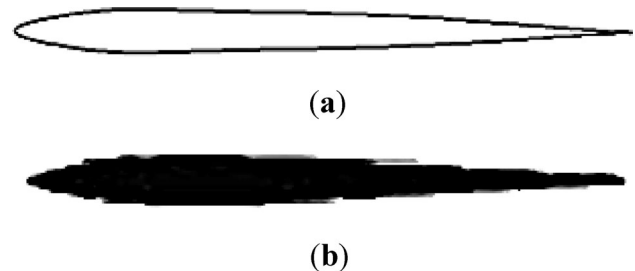








Figure 14. Comparison of optimal airfoil shapes from (a) present computations and (b) Kondoh *et al* [22]; $Re = 2000$.

present study are shown in table 2. The characteristic traits of the optimal airfoil shapes in the ultra-low Re regime are a profile with rather sharp leading edge, $t/c = 4.6\%$ for $Re = 1000$ and increasing to 6.4% for $Re = 10000$. The maximum t/c occurs at about the quarter-chord position for all Re . This information will be useful for designers. Glowinski and Pironneau [23] had shown that the optimal profile has a t/c about 10%. Since, however, we started from an eight percent thick profile, the present optimal t/c values are about 5 to 6%. A sharp leading edge is also not entirely unanticipated in the low Re regime. Previous studies [22–24] have indeed produced optimal airfoil shapes with sharp leading edges.

5.2 Maximizing C_l at $\alpha = 2^\circ$

The next objective function considered is maximizing C_l at $\alpha = 2^\circ$. For this objective function and maximizing (C_l/C_d) objective function considered in the next section the following constraints were imposed. The leading and trailing edges of the airfoil were fixed to maintain the desired α . The upper and lower surfaces of the airfoil were maintained in

Table 2. Summary of C_d of initial and optimal airfoils.

Re	C_d of initial airfoil (NACA 0008)	C_d of optimal airfoil	Optimal airfoil
1000	0.1103	0.1025	
2000	0.0764	0.0728	
4000	0.0533	0.0511	
6000	0.0433	0.0414	
8000	0.0374	0.0356	
10000	0.0335	0.0319	

such a manner that they do not intersect each other. Further, an upper bound for the upper surface of the airfoil was set to not exceed $(y/c) = 0.1$. With these constraints, the optimization was carried out starting from the NACA 0008 airfoil. The optimal C_l values and airfoil shapes obtained are shown in figure 15. Significant increase in C_l values are obtained at all Re considered. The optimal airfoils have evolved into rather thin profiles with distinct droops near the leading and trailing edges. The leading edge droop varies from about 7.3% for $Re = 1000$ to about 1.9% for $Re = 10000$. This droop occurs at about $x/c = 0.28$. The droop near the trailing edge varies from about 3.4% for $Re = 1000$ to about 2.4% for $Re = 10000$, occurring at $x/c = 0.8$. The maximum thickness of the optimal airfoils was about 6% and

its chordwise location varied from $x/c = 0.1$ for $Re = 1000$ and moving aft till $x/c = 0.23$ for $Re = 10000$. A smooth cavity in between the droops is clearly perceptible on the upper surface of the airfoil near the mid-chord. We shall explain how the flow structure in this cavity enhances the lift of the airfoil. The upper surface cavity slowly diminishes with increasing Re . It is also noted that maximum t/c gradually increases with Re .

We shall consider the $Re = 2000$ case in a little more detail as an illustrative example to discuss the C_l improvement. The streamlines over the optimal airfoils are displayed in figure 16a and the contours of vorticity magnitude in figure 16b. A recirculation region is seen on the upper surface of the optimal airfoil near the mid-chord. This recirculation enhances the suction on the airfoil upper surface and consequently its C_l . The recirculation region slowly disappears with increasing Re . The recirculation region on the lower surface also vanishes with increasing Re . The pressure distribution over the NACA 0008 and the optimal airfoils is plotted in figure 17. The suction peak on the optimal airfoil is much higher than that for the NACA 0008 airfoil. This suction peak occurs at $x/c = 0.218$. The pressure on the lower surface is also higher on the optimal airfoil compared to NACA 0008 airfoil. These clearly lead to a higher C_l .

At this stage of our discussion two important questions need to be addressed. (i) What is the optimum shape obtained when the angle of attack is changed? (ii) What is the optimum shape obtained when a different airfoil is chosen as the starting profile? To answer these questions we performed computations with changed angle of attack, $\alpha = 4^\circ, 6^\circ$ and 8° at $Re = 2000$, and the resulting optimal profiles are shown in figure 18a. The optimal profiles had C_l values of 0.686 (0.264), 0.924 (0.341) and 1.049 (0.353), respectively. The values in parentheses are C_l values of the baseline airfoil at their respective α . The characteristic

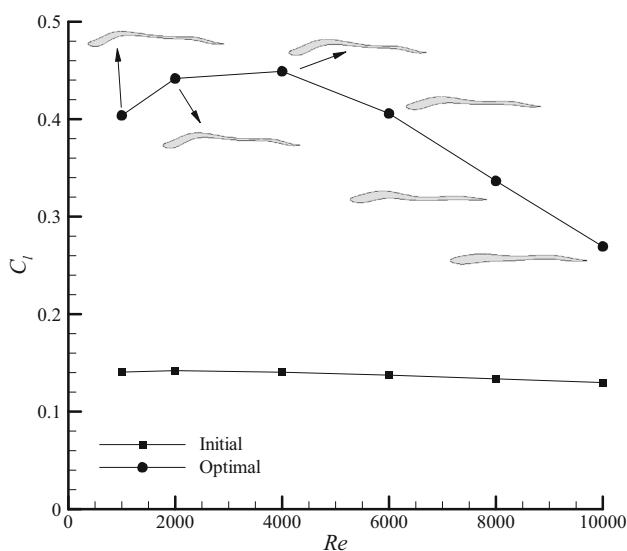


Figure 15. Optimal airfoil shapes for maximizing C_l objective function.

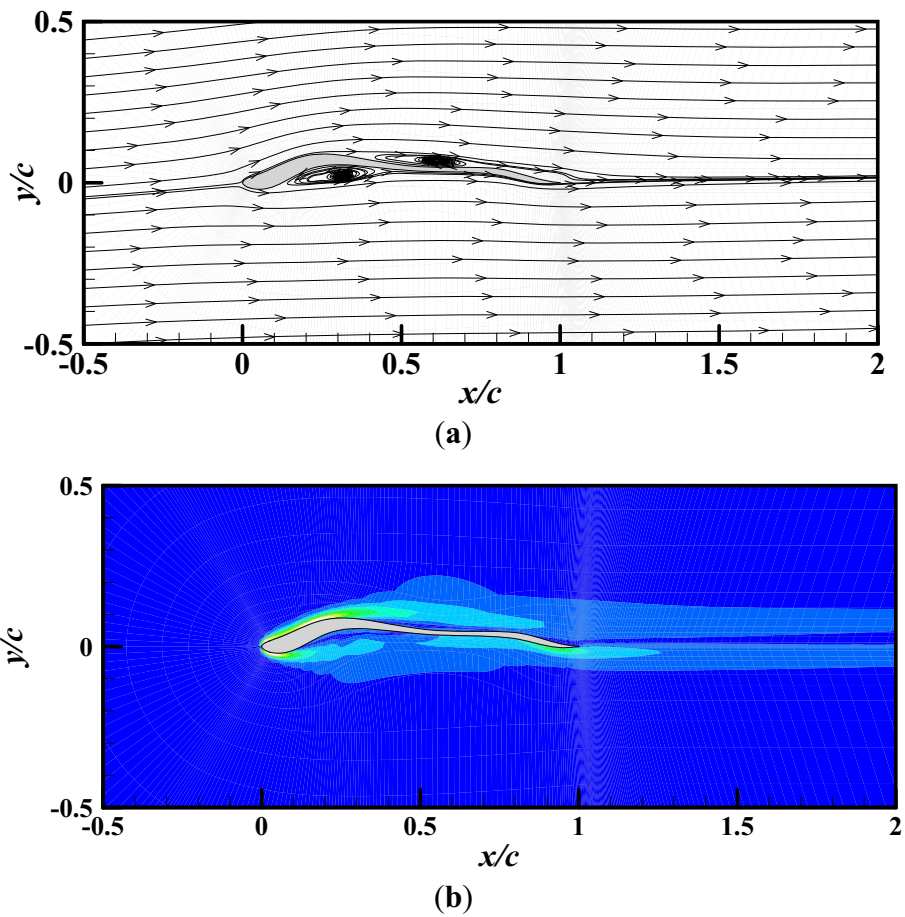


Figure 16. (a) Streamlines, and (b) contours of vorticity magnitude over the optimal airfoil for maximizing C_i ; $Re = 2000$.

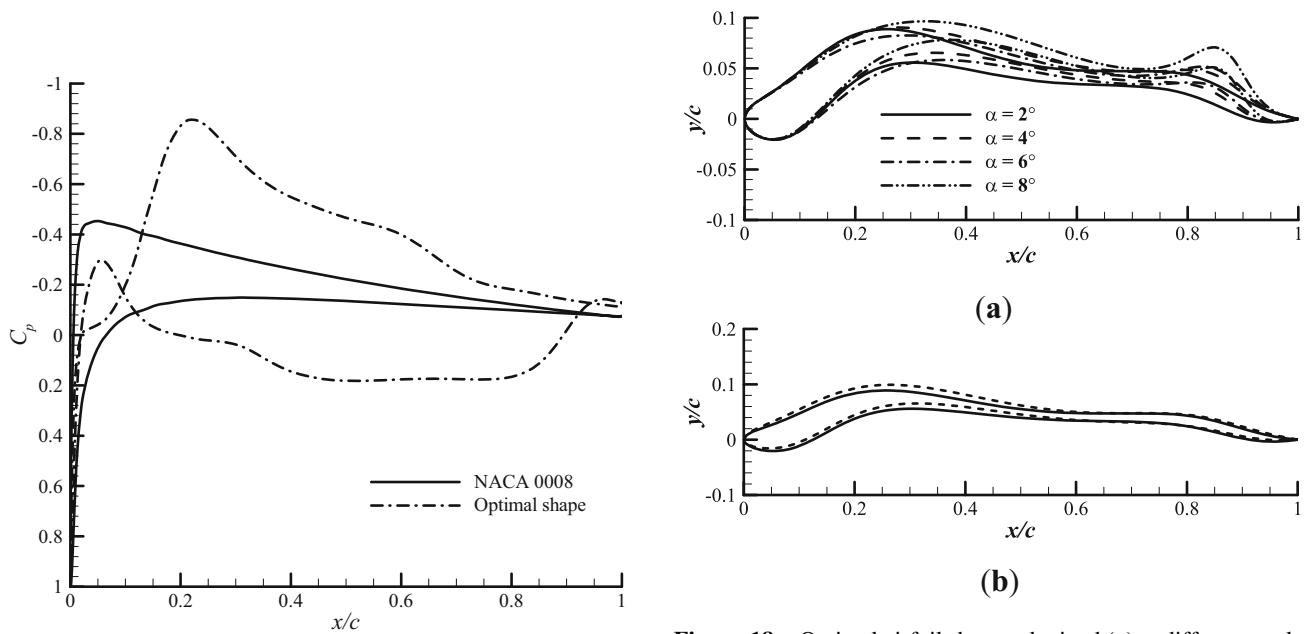


Figure 17. Pressure distribution over NACA 0008 and the optimal airfoils; $Re = 2000$.

Figure 18. Optimal airfoil shapes obtained (a) at different angles of attack, and (b) starting with NACA 0008 (continuous line) and NACA 2408 (dashed line) airfoils; $\alpha = 2^\circ$; $Re = 2000$.

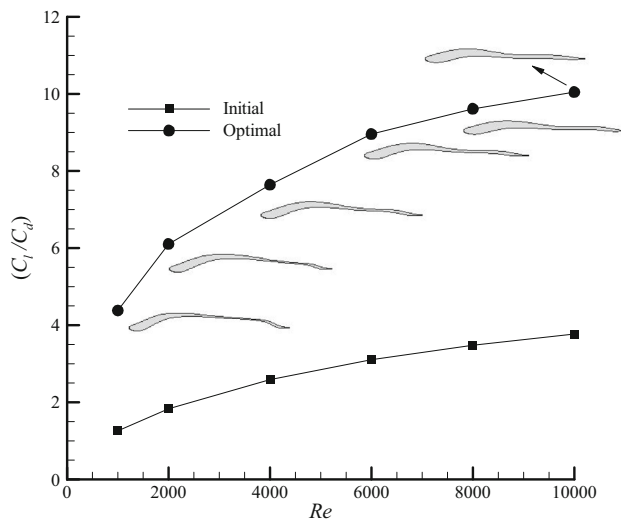


Figure 19. Optimal airfoil shapes for maximizing (C_l/C_d) objective function.

attributes of the optimal shapes can be clearly discerned. Computations were also performed starting from NACA 2408 airfoil for $Re = 2000$, $\alpha = 2^\circ$ and the resulting optimal shape is shown in figure 18b. The optimal airfoil had $C_l = 0.542$ and has similar characteristic features as the optimal airfoil obtained when starting with NACA 0008 airfoil.

5.3 Maximizing (C_l/C_d) at $\alpha = 2^\circ$

The optimal airfoil shapes obtained for maximizing (C_l/C_d) are shown in figure 19. Yet again, we see significant increase in the objective function at all Re considered. The optimal airfoils have similar geometric features as obtained with the C_l maximization objective function. The maximum thickness of the optimal airfoils was about 6% occurring at about $x/c = 0.10$ for $Re = 1000$ and moves slightly rearward to $x/c = 0.14$ for $Re = 10000$. The optimal airfoils have droops near the leading and trailing edges. The leading edge droop varies from about 7.9% occurring at $x/c = 0.34$ for $Re = 1000$ to about 3.8% at $x/c = 0.30$ for $Re = 10000$. The droop near the trailing edge varies from about 4.7% at $x/c = 0.80$ for $Re = 1000$ to 1.4% at $x/c = 0.75$ for $Re = 10000$. A cavity is formed between the droops.

As earlier, the $Re = 2000$ case is considered as an illustrative example. The streamlines and contours of vorticity magnitude over the optimal airfoil are plotted in figure 20. The recirculation region on the airfoil upper surface leads to C_l enhancement. A recirculation region is also seen on the lower surface of the airfoil near the leading edge. These recirculation regions persist till $Re = 10000$. The pressure distribution over the NACA 0008 and the optimal airfoils is plotted in figure 21.

Some comments regarding the optimal airfoil shapes obtained in the literature in the very low Re range are in place here. The optimization study of Kunz and Kroo [11] utilized the camber line as the design element represented by four control points, and using Nelder-Mead simplex procedure at $Re = 2000$ and 6000 resulted in a 5% and 4% increment in $(C_l/C_d)_{\max}$, respectively, compared to the NACA 4702 airfoil. Of interest here is the appearance of the two prominent droops, as also seen in the present study, in their optimal airfoils. However, their geometric parametrization of the camber line precludes the appearance of cavity in between the droops. Our earlier study [25] adopting the approach of Kunz and Kroo [11] resulted in $(C_l/C_d)_{\max} = 4.95$ at $Re = 2000$. The optimization procedure was extended using the fixed-direction set method (a variant of Powell's direction set method) leading to a small further increment in $(C_l/C_d)_{\max}$. In a later study [26] using the same method we parametrized a modified NACA 2408 airfoil using 12 control points; initializing the fixed-direction set optimization procedure from this airfoil we obtained $(C_l/C_d)_{\max} = 3.96$ at $Re = 1000$. Further, optimizing the airfoil upper surface alone, keeping a flat lower surface, we obtained $(C_l/C_d)_{\max} = 4.67$. In these studies the resulting optimal airfoils had a corrugation on the upper surface. Srinath and Mittal [27] performed a comprehensive study to obtain optimal airfoil shapes at $Re \in [10, 500]$ with and without area constraints on the airfoil for five different objective functions. They achieved significant improvements in the aerodynamic performance for all the objective functions considered. Increasing the number of design variables led to a richer design space and better aerodynamic characteristics. The later study of Kumar *et al* [28] maximizing time-averaged lift coefficient resulted in C_l as high as 1.356 at $Re = 1000$, and $C_l = 1.394$ at $Re = 10000$; $\alpha = 4^\circ$ in both the cases. Such high values of C_l were obtained by progressively increasing the number design variables in the design cycle. Their optimal profiles had striking corrugations on the upper surface of the airfoil. The recent study of Lei and He [29] had achieved an optimal (C_l/C_d) of 10.54 at $Re = 10000$, $\alpha = 4^\circ$.

The optimal airfoil shapes for maximizing C_l and maximizing (C_l/C_d) have characteristic droops and a corrugation on the upper surface. It must be appreciated that the corrugation evolves rather naturally during the shape evolution. Though biologically inspired corrugated airfoils have been specifically studied earlier [30–35], achieving corrugated airfoils as optimal profiles via an optimization procedure is indeed remarkable. Nature has an excellent example of corrugated lifting surface in dragonflies. All these point to the importance of corrugations in enhancing the aerodynamic characteristics at ultra-low Reynolds numbers and will have significance in engineering biomimicking flight.

Before we conclude, we mention that in some MAV applications flapping or rotating type of lifting surfaces are employed. The adjoint-based aerodynamic shape

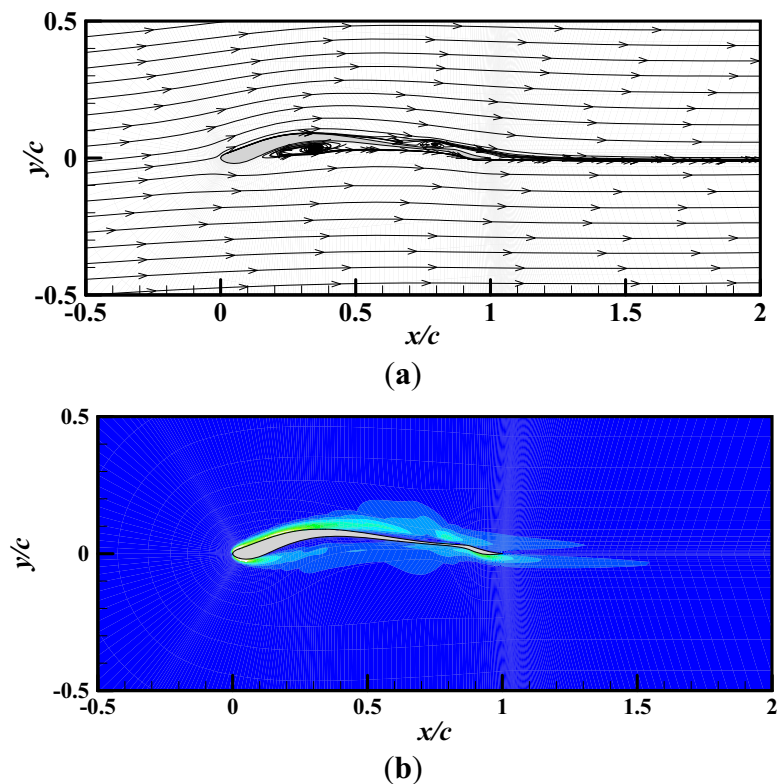


Figure 20. (a) Streamlines, and (b) contours of vorticity magnitude over the optimal airfoil for maximizing (C_l/C_d) ; $Re = 2000$.

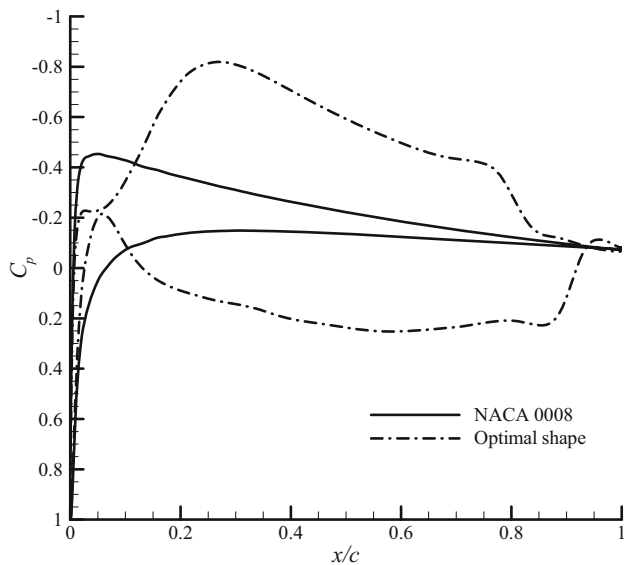


Figure 21. Pressure distribution over NACA 0008 and the optimal airfoils; $Re = 2000$.

optimization framework we have presented in this study can be extended for such applications. For example, when the aerodynamic coefficients change with time a time-averaged objective function can be formulated as

$$J = \frac{1}{T} \int_0^T I(\omega, \zeta) dt, \tag{9}$$

where $I(\omega, \zeta)$ is the now instantaneous value of the objective function and T is period of time averaging.

6. Conclusions

The flow field over NACA 0008 airfoil was studied computationally in the ultra-low Reynolds number regime $Re \in [1000, 10000]$ for various angles of attack $\alpha \in [0^\circ, 8^\circ]$. The flow being laminar it was seen to separate at very small angles of attack. The onset of flow separation is at $\alpha = 6^\circ$ for $Re = 1000$, and occurs at lower α with increasing Re . Once the flow separates, as the angle of attack increases the separation point moves closer to the leading edge. The location of the reattachment point is insensitive to a change in α and remains close to the trailing edge. The slope of the $C_l - \alpha$ curve is lower than inviscid thin airfoil theory value of $C_{l,\alpha} = 2\pi$. Due to early flow separation the maximum C_l obtainable is drastically reduced as compared to the high Reynolds number values. The C_l curve is linear for small α . After flow separation C_l increases non-linearly till the airfoil stalls. It was further seen that higher values of C_l are obtained at lower Re . The separated flow alters the effective

geometry of the airfoil, and consequently its effective camber which is more pronounced at a higher Reynolds number leading to a lower C_l than that achieved at a lower Re . Significant increase in the values of drag coefficient is seen with a decrease in Re . For all the Reynolds numbers considered here the viscous component of drag is significant and it continuously decreases with increasing angle of attack, while the contribution due to pressure drag increases due to flow separation effects. C_l values are low in the ultra-low Re regime, and with high values of C_d , values of (C_l/C_d) are low. This fact provided a motivation for designing airfoils for improved aerodynamic characteristics at low Re .

An adjoint-based aerodynamic shape optimization methodology was employed to obtain improved aerodynamic characteristics in the ultra-low Re regime. Three different objective functions, namely, (i) minimization of drag coefficient, C_d , (ii) maximization of lift coefficient, C_l , and (iii) maximization of lift-to-drag ratio, (C_l/C_d) , were considered. The NACA 0008 airfoil was the initial geometry for the optimization procedure. The characteristic traits of the optimal airfoil shapes obtained in the C_d minimization study are profiles with rather sharp leading edge and maximum t/c of about 5 to 6%. The maximum t/c occurs at about the quarter-chord position for all Re . For the C_l maximization study significant increase in C_l values were obtained at all Re considered. The optimal airfoils were thin profiles with distinct droops near the leading and trailing edges. A smooth cavity was formed in between the droops. The recirculation region in the droop enhances the suction on the airfoil upper surface and consequently its C_l . The (C_l/C_d) maximization study also resulted in significant improvements in the objective function. The resulting optimal airfoils had similar geometric features as those obtained with the C_l maximization objective function.

Notations

A_{ref}	reference area (m^2)
c	airfoil chord length (m)
C_d	coefficient of drag
C_l	coefficient of lift
I	objective function
l_s/c	length of the separated region
p	pressure (Pa)
R	governing equation
Re	Reynolds number
t	time (s)
t/c	thickness-to-chord ratio
\mathbf{u}	velocity vector (m/s)
x, y	Cartesian coordinates
x_r/c	reattachment location
x_s/c	separation location

Greek symbols

α	angle of attack (deg.)
ρ	density (kg/m^3)

ν	kinematic viscosity (m^2/s)
ω	flow field variables
ζ	physical location of the boundary
ψ	Lagrange multiplier

References

- [1] Pines D J and Bohorquez F 2006 Challenges facing future micro-air-vehicle development. *J. Aircr.* 43: 290–305
- [2] Petricca L, Ohlckers P and Grinde C 2011 Micro- and nano-air vehicles: state of the art. *Int. J. Aerospace Eng.* 214549
- [3] Wood R J, Finio B, Karpelson M, Ma K, Pérez-Arancibia N O, Sreetharan P S, Tanaka H and Whitney J P 2012 Progress on “pico” air vehicles. *Int. J. Robot. Res.* 31: 1292–1302
- [4] Carmichael B H 1981 *Low Reynolds number airfoil survey: Vol. I*, NASA CR 165803
- [5] Lissaman P B S 1983 Low-Reynolds-number airfoils. *Ann. Rev. Fluid Mech.* 15: 223–239
- [6] Mueller T J and DeLaurier J D 2003 Aerodynamics of small vehicles. *Ann. Rev. Fluid Mech.* 35: 89–111
- [7] Shyy W, Lian Y, Tang J, Viieru D and Liu H 2008 *Aerodynamics of low Reynolds number flyers*. Cambridge University Press, Cambridge, UK
- [8] Selig M UIUC Low-Speed Airfoil Tests. http://m-selig.ae.illinois.edu/uiuc_lsaf.html
- [9] Thom A and Swart P 1940 The forces on an aerofoil at very low speeds. *J. R. Aeronaut. Soc.* 44: 761–770
- [10] Sunada S, Yasuda T, Yasuda K and Kawachi K 2002 Comparison of wing characteristics at an ultralow Reynolds number. *J. Aircr.* 39: 331–338
- [11] Kunz P J and Kroo I 2001 Analysis and design of airfoils for use at ultra-low Reynolds numbers. In: *Fixed and flapping wing aerodynamics for Micro Air Vehicle applications*, Mueller T J (ed.) AIAA, Virginia
- [12] Mateescu D and Abdo M 2010 Analysis of flows past airfoils at very low Reynolds numbers. *J. Aerosp. Eng.* 224: 757–775
- [13] Hicks R M and Henne P A 1978 Wing design by numerical optimization. *J. Aircr.* 15: 407–412
- [14] Pironneau O 1974 On optimum design in fluid mechanics. *J. Fluid Mech.* 64: 97–110
- [15] Jameson A 1988 Aerodynamic design via control theory. *J. Sci. Comput.* 3: 233–260
- [16] Giles M B and Pierce N A 2000 An introduction to the adjoint approach to design. *Flow Turbul. Combust.* 65: 393–415
- [17] Mohammadi B and Pironneau O 2004 Shape optimization in fluid mechanics. *Ann. Rev. Fluid Mech.* 36: 255–279
- [18] Celik I B, Ghia U, Roache P J, Freitas C J, Coleman H and Raad P E 2008 Procedure for estimation of uncertainty due to discretization in CFD applications. *J. Fluids Eng.* 130: 078001
- [19] Pranesh C, Sivapragasam M and Deshpande M D 2014 Aerodynamic characteristics of flow past NACA 0008 airfoil at very low Reynolds numbers. *J. Aerosp. Sci. Technol.* 66: 247–266
- [20] McCullough G B 1955 The effect of Reynolds number on the stalling characteristics and pressure distributions of four moderately thin airfoil sections. NACA TN-3524
- [21] Petrone G and Hill D C 2014 Single-objective and multi-objective robust optimization of airfoils using adjoint solutions. *AIAA Paper No.* 2014-3173

- [22] Kondoh T, Matsumori T and Kawamoto A 2012 Drag minimization and lift maximization in laminar flows via topology optimization employing simple objective function expressions based on body force integration. *Struct. Multidiscip. Optim.* 45: 693–701
- [23] Glowinski R and Pironneau O 1975 On the numerical computation of the minimum-drag profile in laminar flow. *J. Fluid Mech.* 72: 385–389
- [24] Huan J and Modi V 1996 Design of minimum drag bodies in incompressible laminar flow. *Inverse Probl. Eng.* 3: 233–260
- [25] Dheepak A, Sivapragasam M and Deshpande M D 2015 Airfoil optimisation at a very low Reynolds number. In: *17th Annual CFD Symposium*, Bangalore
- [26] Varsha N 2016 *Optimisation of very low Reynolds number airfoil*. M.Tech. thesis, M S Ramaiah Univeristy of Applied Sciences, Bengaluru
- [27] Srinath D N and Mittal S 2012 Optimal airfoil shapes for low Reynolds number flows. *Int. J. Numer. Methods Fluids* 61: 355–381
- [28] Kumar N, Diwakar A, Attree S K and Mittal S 2012 A method to carry out shape optimization with a large number of design variables. *Int. J. Numer. Methods Fluids* 71: 1494–1508
- [29] Lei J and He J 2016 Adjoint-based aerodynamic shape optimization for low Reynolds number airfoils. *J. Fluids Eng.* 138: 021401
- [30] Kesel A B 2000 Aerodynamic characteristics of dragonfly wing sections compared with technical aerofoil. *J. Exp. Biol.* 203: 3125–3135
- [31] Vargas A, Mittal R and Dong H 2008 A computational study of the aerodynamic performance of a dragonfly wing section in gliding flight. *Bioinspir. Biomim.* 3: 1–13
- [32] Hu H and Tamai M 2008 Bioinspired corrugated airfoil at low Reynolds numbers. *J. Aircr.* 46: 2068–2077
- [33] Murphy J T and Hu H 2010 An experimental study of a bio-inspired corrugated airfoil for MAV applications. *Exp. Fluids* 49: 531–546
- [34] Levy D E and Seifert A 2009 Simplified dragonfly airfoil aerodynamics at Reynolds numbers below 8000. *Phys. Fluids* 21: 071901
- [35] Levy D E and Seifert A 2010 Parameter study of simplified dragonfly airfoil geometry at Reynolds number of 6000. *J. Theor. Biol.* 266: 691–702